

Research on a deformation monitoring model for landslide bodies in reservoir areas of hydropower stations based on distributed fiber optic sensing technology

Lei Lei^{1,2}, Zihao Wu², Yiqing Shi³, Ge Guo³, Qingyun Chen^{1,2,*} and Liang Wang^{1,2}

¹ State Grid (Xi'an) Environmental Protection Technology Center Co., Ltd., Xi'an, Shaanxi, 710100, China

² Electric Power Research Institute of State Grid Shaanxi Electric Power Co., Ltd., Xi'an, Shaanxi, 710100, China

³ State Grid Shaanxi Electric Power Co., Ltd., Xi'an 710048, Shaanxi, China

Corresponding authors: (e-mail: ep_Environmental@163.com).

Abstract Landslide deformation monitoring data are the most significant parameters reflecting the occurrence, development, and evolution of landslides, and serve as essential foundational data for landslide monitoring and early warning systems. This paper establishes a deformation monitoring model for landslide bodies in reservoir areas of hydropower stations based on the displacement sensing theory and computational methods of fiber optic sensing technology and fiber optic grating sensors, addressing the stability and reliability of data monitoring under harsh natural environments and strong electromagnetic interference. By monitoring changes in fiber strain, surface deformation of the slope is calculated. The feasibility of the monitoring model is validated through engineering examples. Experimental results show that the fiber network is highly sensitive to surface deformation caused by suspended loads and can accurately analyze abnormal regions and strain magnitudes. Additionally, the monitoring system can continuously and uninterruptedly track the experimental area, accurately detecting significant displacement of the Xinhua landslide body. Through on-site engineering practice, optical fibers were buried within the slope body and fixed on the slope surface to directly sense slope deformation. It was found that optical fiber strain is significantly influenced by temperature.

Index Terms optical fiber sensing technology, landslide deformation monitoring, conjugate beam method

I. Introduction

Hydropower stations are crucial facilities for alleviating China's electricity shortages and promoting national economic and social development. Landslides are a common geological hazard in hydropower reservoir areas, and their potential harm to power supply, human life, and property should not be underestimated [1]-[4]. To ensure the safe operation of hydropower stations, monitoring the deformation of landslide bodies in reservoir areas is of utmost importance [5].

Traditional monitoring methods primarily utilize electromagnetic sensors and instruments, which are susceptible to electromagnetic interference and cannot perform real-time online monitoring. In contrast, fiber-optic sensors offer advantages such as electromagnetic interference resistance, compact size, lightweight design, corrosion resistance, and high sensitivity [6]-[9]. In recent years, with the rapid development of fiber-optic sensing technology, its application in landslide deformation monitoring has gradually gained traction [10]. Fiber optic sensing technology is a sensing technology based on optical principles, utilizing the unique properties of optical fibers to measure changes in optical signals to obtain measurement variables [11]-[13]. In fiber optic sensing technology, a section of optical fiber is divided into very short segments, each of which acts as a miniature sensor [14], [15]. When physical quantities (such as temperature or strain) act on these sensors, they cause changes in the optical properties of the sensor, such as changes in light intensity or phase, thereby generating optical signals [16]-[18]. Through optical equipment, these optical signals can be measured and converted into corresponding physical quantities, thereby obtaining information about the measured physical quantities [19], [20]. The primary technologies for landslide deformation monitoring using fiber optic sensing include distributed fiber optic sensing technology and fiber Bragg grating technology [21]. Among these, distributed fiber optic sensing technology integrates signal transmission and sensing into a single medium, enabling fully distributed measurements across the entire fiber length of tens or even hundreds of kilometers [22]-[24]. Currently, the most widely applied technologies for long-distance distributed temperature and strain measurements in fiber optic sensing are based on Brillouin optical time-domain reflectometry (BOTDR) and Brillouin optical time-domain analysis (BOTDA) [25]-[27].

Literature [28] summarizes the advantages of distributed fiber optic sensing (DFOS) in landslide monitoring, examines the sensing principles of fiber optics and various DFOS technologies, and analyzes the challenges and development prospects associated with DFOS sensing. Reference [29] discusses the experimental application of distributed fiber optic sensors based on stimulated Brillouin scattering (SBS), demonstrating that the sensors can reveal soil changes prior to debris flow damage and achieve soil crack monitoring to prevent landslides. Reference [30] describes the application of fiber optic sensors in dam and embankment monitoring, systematically introduces different fiber optic sensing technologies and corresponding sensors, and validates the aforementioned application scenarios. Literature [31] employs a distributed fiber optic sensing system to conduct landslide strain measurements on slopes, identifying several stages of landslide evolution and noting that fiber optics can detect precursory signs of failure prior to landslide occurrence, laying the foundation for developing more effective early warning systems. Literature [32] points out that gravity dams, reservoirs, and other structures present numerous challenges for engineers, particularly in terms of operation, maintenance, and inspection, and emphasizes the shortcomings of traditional detection technologies. It proposes reliable, cost-effective sensors based on distributed fiber optic technology. Literature [33] highlights that large-scale active landslides in the upper reaches of the Jinsha River severely hinder the development and utilization of water resources, stressing the necessity of investigating the spatial distribution and deformation trends of active landslides. It also explains the effectiveness of combining interferometric synthetic aperture radar technology, optical satellite imagery, and unmanned aerial vehicle (UAV) photography in identifying landslides. Literature [34] introduces the working principle, characteristics, and application scope of DFOS technology, particularly representative monitoring instruments and equipment based on DFOS. Based on monitoring experiments, it demonstrates that DFOS measurements can sensitively capture the dynamic changes of landslides and identifies the challenges and development trends it faces. Literature [35] outlines the advantages of distributed fiber-optic Brillouin sensing technology and, based on experiments, demonstrates that distributed monitoring systems can meet the requirements for large-scale, high-precision monitoring and are suitable for long-term dynamic monitoring of slopes. Literature [36] investigates the application of DFOS technology in CO₂ geological sequestration. Based on a literature review, fiber optic principles and applications, and representative monitoring projects, it examines the challenges faced by DFOS technology and proposes solutions. Reference [37] introduces DFOS, discusses its measurement principles and current capabilities, and reveals that DFOS can provide an efficient monitoring system for both short-term and long-term applications, thereby enabling "smart infrastructure." The above studies explore the application of DFOS in landslide monitoring and demonstrate the effectiveness of this technology through experiments, highlighting its advantages in terms of monitoring accuracy, wide coverage, reliability, and cost-effectiveness.

This paper first establishes a dynamic monitoring model. Based on the principles of fiber optic sensing technology and the displacement sensing theory of fiber optic grating sensors, a fiber optic grating sensor tube suitable for monitoring deep-seated displacement in slopes is developed. A conjugate beam calculation method for strain-displacement conversion is proposed, and based on this, a monitoring model for deformation of landslide bodies in reservoir areas of hydropower stations is introduced. Taking the Xinhua landslide body in the Daguangshan reservoir area of the Dadu River as a case study, the monitoring data analysis system automatically processes the monitoring data to obtain real-time monitoring data of the landslide body, understand the status and trend changes of each landslide body, and achieve the objectives of real-time monitoring, forecasting, and early warning.

II. Deformation monitoring model for landslides in hydroelectric reservoir areas

II. A. Dynamic monitoring model for landslide displacement in hydropower reservoir areas

II. A. 1) Establishment of displacement model

For the sake of mathematical description, each sensor monitoring point is regarded as a moving target. Thus, the monitoring process can be regarded as the monitoring of the movement trajectory of each sensor, and its displacement process can be described by Newton's second law of motion:

$$\left. \begin{aligned} s(x+1) &= s(x) + Tv(x) + \frac{1}{2}a(x)T^2 \\ v(x+1) &= v(x) + Ta(x) \end{aligned} \right\} \quad (1)$$

In the equation: $s(x)$ and $v(x)$ represent the position and velocity of the landslide monitoring point at time x ; $a(x)$ is the acceleration caused by external factors between time x and $x+1$ at the monitoring point, which takes into account the unpredictable behavior caused by the landslide displacement itself and external environmental disturbances. $a(x)$ is a process noise sequence that follows a normal distribution with a mean of zero and a variance of Q , and $a(x)$ and $a(y)$ ($x \neq y$) are uncorrelated, i.e., $E\{a(x)\} = 0$ and $E\{a(x)a(y)\} = Q\delta(x-y)$,

where δ is the Kronecker delta function, which has the property that $\delta(k)=1$ when $k=0$ and $\delta(k)=0$ when $k=1$.

II. A. 2) Establishment of a dynamic monitoring model and determination of weight values

If the displacement and velocity of landslide monitoring points are regarded as state variables of landslides, then based on the above analysis, state equations (equivalent to theoretical calculation models) and actual measurement equations for landslides in the deformation stage can be established, i.e., dynamic monitoring models:

$$\left. \begin{aligned} X(k+1) &= \Phi(k)X(k) + \Gamma(k)W(k) \\ Z(k) &= H(k)X(k) + V(k) \end{aligned} \right\} \quad (2)$$

Among them,

$$X(k) = \begin{Bmatrix} s(k) \\ v(k) \end{Bmatrix} \quad (3)$$

$$\Phi(k) = \begin{bmatrix} 1 & T \\ 0 & T \end{bmatrix} \quad (4)$$

$$H(k) = \{1 \quad 0\} \quad (5)$$

$$\Gamma(k) = \begin{Bmatrix} T^2 / 2 \\ T \end{Bmatrix} \quad (6)$$

$$W(k) = a(k) \quad (7)$$

In the equation: $V(k)$ is a measurement noise sequence with a mean of zero and variance of Q , and is uncorrelated with $W(k)$; $Z(k)$ is the actual displacement monitoring value of the dam foundation, which includes various external interference factors affecting the monitoring (i.e., noise).

When determining the weight values for each set of monitoring data, a multi-group experimental method is used for calculation, with the calculation method as follows:

$$\sigma = \sqrt{\frac{1}{n-1} \sum_{i=1}^n (x_i - \bar{x})^2} \quad (8)$$

In the formula: σ is the variance of the data, x_i is the i th measurement under the same conditions, and \bar{x} is the average value of all measurements.

Considering the case where m sensors directly observe a one-dimensional target, the observation equation is:

$$z_i(k) = x(k) + v_i(k) \quad (k=1, 2, \dots, n; i=1, 2, \dots, m) \quad (9)$$

In the equation: n is the signal length, m is the number of sensors, $z_i(k)$ is the observation value of sensor i at time k , $x(k)$ is the target state to be estimated, and $v_i(k)$ is the observation noise of sensor i at time k .

When no other information is available and x can only be determined from the observations, its optimal estimate \hat{x} should be the linear weighted average of all observations. For any number of sensors making observations, i.e.:

$$\hat{x} = k_1 z_1 + k_2 z_2 + \dots + k_m z_m \quad (10)$$

Seeking the optimal estimate under the condition of minimum mean square error, the problem is transformed into finding an unbiased estimate of x such that the mean square error of the estimate is minimized. Estimated error:

$$\bar{x} = x - \hat{x} = x - (k_1 z_1 + k_2 z_2 + \dots + k_m z_m) \quad (11)$$

The unbiasedness requirement of the estimate is $E(\bar{x}) = E[x - k_1(x + v_1) - k_2(x + v_2) - \dots - k_m(x + v_m)] = 0$, so it must be:

$$k_1 + k_2 + \dots + k_m = 1 \quad (12)$$

Since v_i is independent, the estimated standard deviation of the error is:

$$\begin{aligned} E(\bar{x}^2) &= E \left\{ \left[\left(1 - \sum_{i=1}^m k_i \right) x + \sum_{i=1}^m k_i v_i \right]^2 \right\} \\ &= \sum_{i=1}^m (k_i^2 \sigma_i^2) = \sum_{i=1}^{m-1} (k_i^2 \sigma_i^2) + \left(1 - \sum_{i=1}^{m-1} k_i \right)^2 \sigma_m^2 \end{aligned} \quad (13)$$

In order to obtain the optimal estimate of the target signal under the condition of minimum mean square error, it is only necessary to appropriately select k_i so that $E(\bar{x}^2)$ is minimized. The solution is obtained as follows:

$$k_i = \frac{\det(A_i)}{\det(A)} \quad (14)$$

Among them,

$$A = \begin{bmatrix} \sigma_1^2 + \sigma_m^2 & \sigma_m^2 & \dots & \sigma_m^2 \\ \sigma_m^2 & \sigma_2^2 + \sigma_m^2 & & \sigma_m^2 \\ \vdots & & \ddots & \vdots \\ \sigma_m^2 & \sigma_m^2 & \dots & \sigma_{m-1}^2 + \sigma_m^2 \end{bmatrix}_{(m-1)(m-1)} \quad (15)$$

$$b = \{\sigma_m^2, \sigma_m^2, \dots, \sigma_m^2\}^T \quad (16)$$

In the formula: A_i is the matrix obtained by replacing the i th column of A with b . Calculating the corresponding determinant value yields:

$$k_i = \prod_{\substack{j=1 \\ j \neq i}}^m \sigma_j^2 \bigg/ \sum_{s=1}^m \prod_{\substack{j=1 \\ j \neq s}}^m \sigma_j^2 \quad (i=1, 2, \dots, m) \quad (17)$$

II. B. Principles of Fiber Optic Monitoring Technology

II. B. 1) Distributed Fiber Optic Sensing Technology

Due to the harsh on-site monitoring environment and severe electromagnetic interference, the project employs fiber optic sensors for monitoring. Compared to traditional sensors based on electrical measurement principles, fiber optic grating sensors offer the following advantages:

1) They are unaffected by humid environments, can avoid electromagnetic field interference, have excellent electrical insulation properties, are corrosion-resistant, and can withstand high temperatures, effectively preventing lightning strikes, electromagnetic interference, and other issues.

2) They have good durability and can withstand harsh environments, including high temperatures, and chemical corrosion.

3) They are lightweight, compact, have minimal structural impact, are easy to install, and are easy to process.

4) They can perform both point measurements and distributed measurements, form multiplexed systems, and are easy to network.

Fiber optic sensors typically consist of a light source, transmission fiber, sensing elements or modulation zones, and light detectors. Their operating principle is based on the optical modulation effect of optical fibers, i.e., when external environmental factors (such as temperature, pressure, electric field, magnetic field, etc.) change, the optical transmission characteristics (such as phase and intensity) of the fiber also change. In other words, if the changes in the phase and intensity of light passing through the fiber can be measured, the changes in the physical quantity being measured can be determined [38]. A fiber Bragg grating refers to a new type of fiber-based Bragg grating formed by exposing single-mode germanium-doped fiber to ultraviolet light. After grating formation, the refractive index of the fiber core exhibits periodic distribution stripes and produces the Bragg grating effect. For fiber Bragg gratings, when broadband light propagates through the FBG, mode coupling occurs, and a narrowband spectrum that satisfies the Bragg condition is reflected back. The Bragg condition is:

$$\lambda_B = 2n_{eff}\Lambda \quad (18)$$

In the equation: λ_B is the Bragg wavelength; n_{eff} is the effective refractive index of the fiber core region; Λ is the Bragg grating period of the fiber.

When the parameters measured by the fiber Bragg grating change, it leads to changes in the fiber Bragg grating's n_{eff} or Λ , thereby causing changes in the fiber Bragg grating's reflection wavelength λ_B . Therefore, by measuring changes in the central reflection wavelength of the fiber Bragg grating, one can obtain information about changes in the physical quantity being measured. The acquisition of the central wavelength and its working principle are shown in Figure 1.

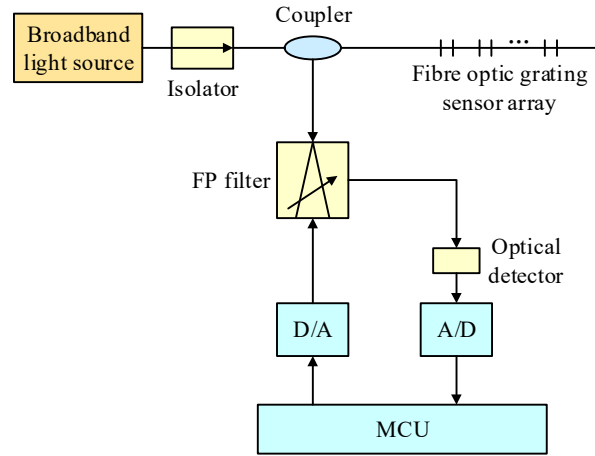


Figure 1: Fiber optic grating sensing principle diagram

The light emitted by the broadband light source is coupled into the fiber Bragg grating sensor array via a coupler, reflected by each fiber Bragg grating, and then transmitted to the FP (Fabry-Perot) filter via the coupler. When the detector detects the light signal, the transmission wavelength of the filter is equal to the reflection wavelength of the fiber Bragg grating.

When the FBG is simultaneously subjected to varying measured quantities and varying temperatures, the wavelength change of the fiber Bragg grating is $\Delta\lambda_B$, then:

$$\frac{\Delta\lambda_B}{\lambda_B} = (1 - P_c) \Delta\varepsilon_f + (\alpha_s + \zeta_s) \Delta t \quad (19)$$

In the equation: P_c is the effective photoelastic coefficient; $\Delta\varepsilon_f$ is the environmental quantity of FBG change; α_s is the thermal expansion coefficient of the optical fiber; ζ_s is the thermo-optic coefficient; Δt is the temperature change quantity. And:

$$P_c = \frac{n_{eff}^2}{2} ((1 - \nu) P_{12} - \nu P_{11}) \quad (20)$$

In the equation: ν is the Poisson's ratio of the fiber core material; P_{11} and P_{12} are the Puckel coefficients of the photoelastic tensor.

II. B. 2) Fiber Bragg Grating Strain Sensing Principle

A Prague Fiber Bragg Grating (FBG) is a special type of fiber optic grating that is etched onto the core of a single-mode fiber. It is small in size, typically only a few millimeters in diameter, and is a miniature, non-contact, scalable, reusable, and multifunctional device [39]. Its operating principle involves illuminating a horizontally placed optical fiber with a beam of ultraviolet laser light. Using phase mask technology, interference patterns generated within the core of the single-mode optical fiber can be observed. Since the core material of the optical fiber is a silica matrix, exposure to the ultraviolet laser beam causes permanent, irreversible changes in the fiber's physical properties, resulting in the formation of permanent, periodic refractive index modulation within the core.

FGB can be specially engraved to make its refractive index n_0 exhibit periodic changes, and the period can be adjusted.

$$n_{eff} = n_0 + \Delta n^* [1 + \cos(2\pi x) / \Lambda] \quad (21)$$

In the equation: x is the fiber core axis; Δn^* is the refractive index modulation.

In a Bragg grating, the wavelength changes with changes in stress and temperature. The change can be expressed by the following equation:

$$\Delta\lambda_B = \left\{ \left[(1 - P_e) \varepsilon + \left(\alpha_f + \left(\frac{dn_{eff}}{dT} \right) / n_{eff} \right) \Delta T \right] \right\} \lambda_B \quad (22)$$

In the formula: $\Delta\lambda_B$ represents the wavelength change of the fiber Bragg grating; P_e represents the effective photonic coefficient of the fiber Bragg grating; ε is the strain; α_f is the thermal expansion coefficient of the FBG;

$\frac{dn_{eff}}{dT} = \xi$ is the refractive index-temperature coefficient of the FBG, i.e., the thermal optical coefficient of the FBG material; ΔT refers to the external temperature.

When $K_\varepsilon = 1 - p_e$, K_ε is the strain sensitivity coefficient, and when $K_T = \left(\frac{1}{n_{eff}} \xi + \alpha_f \right)$, K_T is the temperature sensitivity coefficient, equation (22) can be expressed as:

$$\frac{\Delta\lambda_B}{\lambda_B} = K_\varepsilon \varepsilon + K_T \Delta T \quad (23)$$

According to Formula (23), a Bragg grating is an optical component that combines temperature sensitivity and stress sensitivity. Its dimensions change with variations in temperature and stress, thereby altering its wavelength.

During the process of measuring and adjusting external temperature, the FBG sensor must maintain zero tension. Therefore, changes in the refractive index of the fiber can clearly describe the changes in the wavelength of the reflected light when affected by temperature. During the process of testing and adjusting external stress, it is necessary to ensure that there is a temperature effect in the FBG. To avoid cross-effects of temperature on stress testing at the grating wavelength, a separate grating with zero tensile stress is typically installed next to the strain sensor to test temperature independently. The wavelength drift obtained from the strain sensor is then subtracted from the drift caused by temperature effects. This process is also known as temperature compensation, ultimately yielding the strain value caused by strain.

II. C. Fiber optic grating sensor tube displacement sensing principle

II. C. 1) Temperature Compensation Issues

To overcome the interference of temperature effects on measurement results, it is common to introduce other forms of stress into the fiber optic grating to enable real-time measurement of temperature effects. Although this method is highly effective in indoor model tests, in actual measurements, the temperature of deep rock and soil in slopes varies inconsistently over time and space, and differs significantly from surface temperatures. To further eliminate temperature effects, temperature compensation is applied to the deformation pipe. In this study, two transducers are respectively placed at the upper and lower symmetrical positions on the pipe. The wavelength drift value of the FBG at any cross-section varies with external stress and temperature changes and can be expressed by the following formula:

$$\frac{\Delta\lambda_{wFBGi}}{\lambda_B} = K_T \Delta T + K_\varepsilon \varepsilon_{wFBGi} \quad (24)$$

$$\frac{\Delta\lambda_{wFBGi'}}{\lambda_B} = K_T \Delta T + K_\varepsilon \varepsilon_{wFBGi'} \quad (25)$$

In the equation: $\Delta\lambda_{wFBGi}$ and $\Delta\lambda_{wFBGi'}$ are the wavelength shifts of the FBG symmetrically arranged on the deformed tube wall; ε_{wFBGi} and $\varepsilon_{wFBGi'}$ are the corresponding strain values applied to the FBG symmetrically placed on the deformed tube surface.

Combining (24) and (25), the effect of temperature on FBG stress can be excluded and expressed as:

$$\frac{\Delta\lambda_{wFBGi} - \Delta\lambda_{wFBGi'}}{\lambda_B} = K_\varepsilon (\varepsilon_{wFBGi} - \varepsilon_{wFBGi'}) \quad (26)$$

II. C. 2) Principle of displacement sensing

When the FGB strain tube undergoes deformation, the relationship between the strain $\varepsilon(x)$ at any point on a cross section and the curvature radius $\rho(x)$ can be expressed as:

$$\frac{\varepsilon(x)}{r} = \frac{1}{\rho(x)} \quad (27)$$

where, r is the distance from the measurement point to the center axis of the cross section.

The relationship between the material curvature radius $\rho(x)$ and the deflection value $f(x)$ is:

$$\frac{1}{\rho(x)} = \frac{d^2 f(x)}{dx^2} \quad (28)$$

Further, we obtain the relationship between the deflection $f(x)$ and strain $\varepsilon(x)$ at any point on the deformed tube:

$$f(x) = \frac{1}{r} \iint \varepsilon(x) dx dx \quad (29)$$

Establish quantitative relationships between strain and deflection in the longitudinal direction of the deformed pipe.

II. C. 3) Strain-displacement conversion using the conjugate beam method

The differential equation for the deflection curve of a beam is generally expressed as:

$$\frac{d^2 M(x)}{dx^2} = \frac{dV(x)}{dx} = -q(x) \quad (30)$$

Similarly, the relationship between beam deformation and internal force is as follows:

$$\frac{d^2 w(x)}{dx^2} = \frac{d\theta(x)}{dx} = -\frac{M(x)}{EI} \quad (31)$$

In the formula, $M(x)$, $V(x)$, $q(x)$, $w(x)$, and $\theta(x)$ represent the bending moment, shear force, distributed load intensity, deflection, and slope of the actual beam in the x direction, respectively. EI is the bending stiffness of the beam cross-section.

The simplified diagrams of simply supported beams, cantilever beams, and corresponding conjugate beams are shown in Figure 2. The length of the beam, L , is uniformly distributed bending stiffness, EI , and is divided into n units along the longitudinal direction, denoted as unit 1 to unit n , with a uniform length, $l = L/n$. The two ends of the i th unit have two strain measurement points (the fixed end is defined as the origin), and the curvature at both ends of the i th element can be expressed as:

$$\begin{aligned} k(x_i) &= \frac{M(x_i)}{EI} = \frac{e(x_i)}{z} = q^*(x_i), k(x_{i+1}) \\ &= \frac{M(x_{i+1})}{EI} = \frac{e(x_{i+1})}{z} = q^*(x_{i+1}) \quad (i = 1 \sim n) \end{aligned} \quad (32)$$

The average equivalent load distribution of the i th unit in the composite beam can be expressed as:

$$\bar{q}_i^* = 0.5(q^*(x_i) + q^*(x_{i+1})) = \frac{1}{2z}(\varepsilon(x_i) + \varepsilon(x_{i+1})) \quad (33)$$

(1) For simply supported beams: In structural health monitoring of bridges and buildings, monitoring under random loads can be simplified to simply supported beams. The simply supported beam model is shown in Figure 2(a), and the conjugate conditions of the simply supported beam boundary conditions remain simply supported beams. According to Equation (31), the bending moment at the boundary point between the p th element and the $p+1$ th element ($1 \leq p \leq n-1$) on the conjugate beam (Figure 2(b)) can be easily calculated as follows:

$$\begin{aligned} M^*(x_{p+1}) &= \frac{l}{n} \sum_{i=1}^n \bar{q}_i^* \left(n-i+\frac{1}{2} \right) pl - \left(\frac{1}{2} \bar{q}_p^* l^2 + \left(\frac{1}{2} + 1 \right) \bar{q}_{p-1}^* l^2 \right. \\ &\quad \left. + \left(\frac{1}{2} + 2 \right) \bar{q}_{p-2}^* l^2 + \dots + \left(\frac{1}{2} + p-i \right) \bar{q}_1^* l^2 \right) \\ &= \frac{pl^2}{n} \sum_{i=1}^n \bar{q}_i^* \left(n-i+\frac{1}{2} \right) - l^2 \sum_{i=1}^p \bar{q}_i^* \left(p-i+\frac{1}{2} \right) \\ &= l^2 \left(\frac{p}{n} \sum_{i=1}^n \frac{(\varepsilon(x_i) + \varepsilon(x_{i+1}))}{2z} \left(n-i+\frac{1}{2} \right) \right. \\ &\quad \left. - \sum_{i=1}^p \frac{(\varepsilon(x_i) + \varepsilon(x_{i+1}))}{2z} \left(p-i+\frac{1}{2} \right) \right) \quad (p = 1 \sim n-1) \end{aligned} \quad (34)$$

Substituting $l = L/n$ into equation (34) yields the deflection at the corresponding point of the actual beam:

$$\begin{aligned} w(x_{p+1}) &= M^*(x_{p+1}) \\ &= \frac{L^2}{n^2} \left(\frac{p}{n} \sum_{i=1}^n \frac{(\varepsilon(x_i) + \varepsilon(x_{i+1}))}{2z} \left(n-i+\frac{1}{2} \right) \right. \\ &\quad \left. - \sum_{i=1}^p \frac{(\varepsilon(x_i) + \varepsilon(x_{i+1}))}{2z} \left(p-i+\frac{1}{2} \right) \right) \end{aligned} \quad (35)$$

(2) For cantilever beams: When conducting deep deformation monitoring of rock and soil engineering such as excavation pits and slopes, FGB sensors based on surface-mounted drill holes can be simplified to cantilever beams under random loads. The cantilever beam model has conjugate conditions for cantilever beam boundary conditions as reverse cantilever beams.

$$\begin{aligned}
 M^*(x_{p+1}) &= \frac{1}{2} \bar{q}_p^* l^2 + \left(\frac{1}{2} + 1\right) \bar{q}_{p-1}^* l^2 + \left(\frac{1}{2} + 2\right) \bar{q}_{p-2}^* l^2 \\
 &\quad + \dots + \left(\frac{1}{2} + p - i\right) \bar{q}_1^* l^2 \\
 &= l^2 \sum_{i=1}^p \bar{q}_i^* \left(p - i + \frac{1}{2}\right) \\
 &= l^2 \sum_{i=1}^p \frac{(\varepsilon(x_i) + \varepsilon(x_{i+1}))}{2z} \left(p - i + \frac{1}{2}\right) \quad (p = 1 \sim n - 1)
 \end{aligned} \tag{36}$$

Substituting $l = L/n$ into equation (36) yields the deflection at the corresponding point of the actual beam:

$$\begin{aligned}
 w(x_{p+1}) &= M^*(x_{p+1}) \\
 &= \frac{L^2}{n^2} \sum_{i=1}^p \frac{(\varepsilon(x_i) + \varepsilon(x_{i+1}))}{2z} \left(p - i + \frac{1}{2}\right)
 \end{aligned} \tag{37}$$

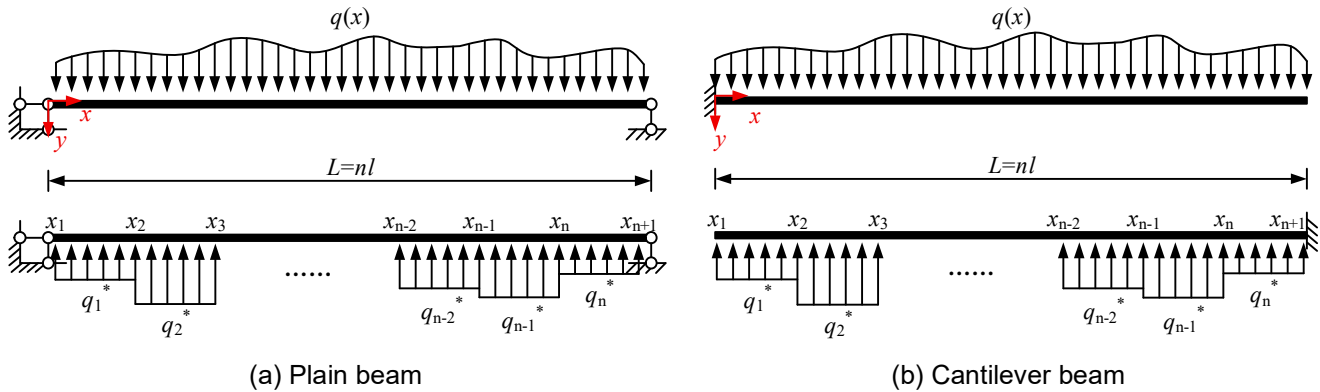


Figure 2: Two kinds of ordinary beams and their corresponding beams

III. Experimental analysis

The strain data collected by the BOTDR strain analyzer is transmitted to the computer via a local area network and saved in text format. Since the data is distributed, each collection contains 10,000 consecutive sampling points, meaning that each file contains 10,000 strain data points distributed continuously along the length of the optical fiber. The first step in experimental analysis is to plot strain curves at 0.1m sampling intervals to visually represent the strain distribution along the fiber.

Before the experiment begins, record the specific positions of the midpoints of each segment of fiber along the fiber length and input the positioning information as shown in Table 1.

Table 1: Each section of the optical fiber point location information

	1	2	3	4	5	6	7	8	9	10	11	12	13	14	15
A	321.1	319.2	316.4	314.7	311.6	311.2	308.1	314.1	307.7	305.2	304.3	301.4	301.5	305.4.3	297.4
B	275.4	277.4	278.5	279.5	275.4	284.5	286.2	288.5	289.7	289.1	290.4	292.4	294.2	296.1	299.4

III. A. Single-node experiment

Figure 3 shows two strain distribution curves of the fiber optic network under different stress conditions. The blue dashed line represents the initial strain of the fiber optic sensor network in its free state prior to the experiment. Due to variations in the force applied during the manual installation of each segment of fiber optic cable, the initial strain of each segment varies significantly, resulting in an uneven curve. The blue solid line represents the strain

distribution after weights were suspended from nodes A4 and B4 in the network. Compared to the light-colored line, the overall strain has slightly increased, with noticeable increases in certain localized areas.

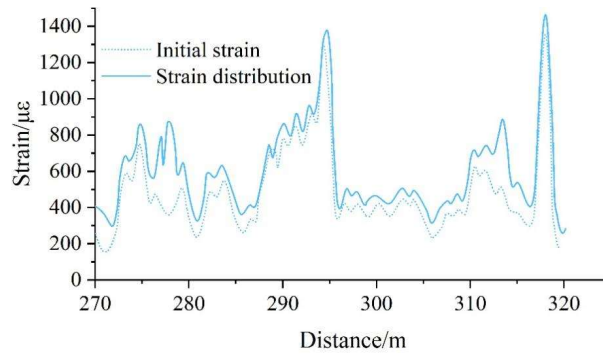


Figure 3: Contrast of the strain measurement lines before and after loading

The overall upward shift in the strain curve is due to changes in environmental temperature. To compensate for the effects of temperature changes on strain measurement results, temperature compensation is required. The specific method involves selecting a section of slack fiber outside the fiber optic network, approximately 2 meters in length. Since this section of slack fiber is not subject to the gravitational force of the weights, its actual strain state remains consistent before and after weight loading. The strain changes measured by the instrument are entirely due to changes in the ambient temperature. Since the slack fiber optic cable and the fiber optic network are in the same temperature field, they are affected by temperature to the same extent. By subtracting the strain change measured by the instrument from the strain curve, the influence of temperature on the strain measurement values of the fiber optic network can be eliminated.

The reason for the significant local increase in the strain curve is due to the local deformation of the fiber optic network under the gravitational force of the 10g weight.

To more intuitively assess the strain differences in the fiber optic network under the gravitational force of the weight, the initial strain is subtracted from the force-induced strain curve, resulting in a new strain distribution curve as shown in Figure 4.

Analyzing the strain distribution curve in the figure, it was found that there are distinct peaks near the 275.9m and 318.5m regions. From the shape of the peaks, the former is slightly higher than the latter, while the latter is slightly wider than the former. Referring to the positioning information, 275.9m is located at the midpoint of fiber B4, and 318.5m is located at the midpoint of fiber A4; fibers A3 and A5 are also affected by B4, with strain values slightly increasing. Therefore, the node coordinates of the suspended weight are A4B4, and the direction of force is from B to A.

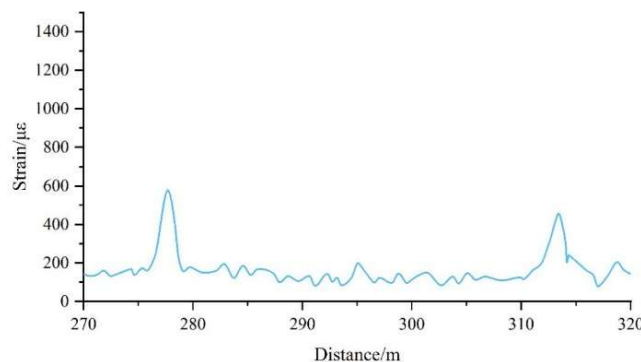


Figure 4: The reduced strain measurement line of fiber optic sensing net loaded at the nodal point of A4B4

III. B. Node cluster experiment

After placing the notebook horizontally in the area near A12B12 to A13B13, the measurement results after deducting the initial value are shown in Figure 5. Analyzing the strain curves in the figure, there are two regions with significantly abnormal strain values. Compared to the single-node experiment, the width and strain values of the abnormal regions are larger. This is primarily because the notebook placed in the node group experiment has a

larger area and a weight significantly greater than the 10g weight, thereby exerting a greater impact on the fiber optic network than the single-node experiment. By comparing the fiber positions in the abnormal regions with the location information obtained from the OTDR, it was found that the abnormalities occurred in the region formed by nodes A12B12, A12B13, A13B12, and A13B13, which aligns with the actual situation. Comparing the widths of the two abnormal regions, it was found that at least six fibers in Group A exhibited abnormalities, while only two fibers in Group B showed abnormalities, indicating that the direction of the force is from B to A.

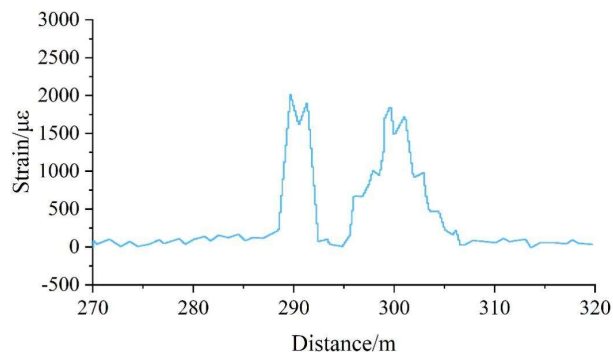


Figure 5: The reduced strain measurement line of fiber optic sensing net loaded at several nodal points

IV. Engineering examples

IV. A. Project Overview and Monitoring Plan

IV. A. 1) Project Overview

The Xinhua landslide is located in Xinhua Village, Detuo Township, on the left bank of the Dadu River between the Tianwan River mouth and Shadang section, 14.6 km from the dam site of the Dagao Mountain Power Station. The elevation of the landslide's leading edge is 1,070 m, while the trailing edge reaches 1,430 m. The landslide measures approximately 610 m in length, 460 m in width, and covers an area of about 27,000 m². The explored thickness ranges from 50 to 70 m, with a volume of approximately 700,000 m³. The landslide developed in the Triassic Baiguowan Formation (T3bg) sandstone and shale. The downstream side is composed of grayish-white to slightly reddish medium-grained biotite diorite granite (γ 24). The landslide body is sandwiched between the eastern and western branches of the Dadu River Fault. A strike-slip fault with a direction similar to the landslide body's distribution is developed at the downstream edge, with a strike of N60°E. The landslide forms a circular chair-shaped terrain, with a landslide platform developed at an elevation of 1,300–1,370 m. The terrain slope is 10°–15°, with a general slope of 30°–40° below, and a shallow gully developed in the middle. The front edge of the landslide body is overlying a grade III terrace gravel layer, with strip-like seepage phenomena along the contact surface. The landslide body is primarily composed of blocky gravelly soil, interspersed with sandstone and shale boulders ranging from several meters to over ten meters in size.

IV. A. 2) Monitoring Plan

Deformation monitoring of the Xinhua landslide body at Dagao Mountain employs GNSS observation methods, including one satellite positioning continuous operation reference station and five deformation monitoring points. The GNSS reference station is established on stable bedrock on the opposite bank (XTP01), while the monitoring points are established on the landslide body. The Xinhua landslide has two GNSS monitoring sections. In the A-A monitoring section, one monitoring point is established at each of the 1,143m, 1,321m, and 1,440m elevations; in the B-B monitoring section, one monitoring point is established at each of the 1,120m and 1,355m elevations. The monitoring points are numbered XP01, XP02, XP03, and XP04.

IV. A. 3) Installation of reference station and monitoring point markers

The benchmark station is located on stable bedrock outside the landslide area where geological conditions are favorable and remain stable throughout the year (on the opposite bank of the landslide body). To ensure the stable and safe operation of the benchmark station throughout the year, a benchmark station observation and protection building has been constructed. The five monitoring points are marked with 8 mm thick, 350 mm diameter, 5 m long galvanized steel pipes filled with concrete. The markers are cast into concrete foundation piers.

IV. B. Analysis of Monitoring Results

To maintain consistency with the coordinate reference system of the hydropower station dam, the reference station XTP01 was linked with three reference points (TN05, TN06, and TN09) in the dam deformation monitoring reference network via GNSS joint measurement. As of 12:00 on August 9, 2023, the statistical data on partial displacement and crack monitoring at the four monitoring points (XP01 to XP04) of the Xinhua landslide body are shown in Table 2. As shown in the table: ① The deformation values at each monitoring point continue to increase, and the deformation rate also increases synchronously; ② The deformation is divided into two regions above and below the highway. The region above the highway has relatively slower deformation, with horizontal displacement of approximately 541–870 mm and subsidence of approximately 372–584 mm during the period from July 23 to August 9; the deformation in the area below the highway is severe, with horizontal displacement ranging from approximately 1,689 to 3,351 mm and settlement ranging from approximately 792 to 1,759 mm during the period from July 23 to August 9, particularly in the XP04 area; ③ the width of cracks on the highway pavement increased by nearly 3 m during the period from July 23 to August 9, with a significant increase in the number of new cracks. The increase in crack length and width indicates severe displacement.

Table 2: Statistical and crack monitoring of partial displacement in each monitoring point

Monitoring point	XP01		XP02		XP03		XP04		Road crack		New fracture			collapse
	Cumulative deformation		Cumulative deformation		Cumulative deformation		Cumulative deformation		Length/m	Width/m	Quantity/bar	Length/m	Width/m	
	Level	Perp.	Level	Perp.	Level	Perp.	Level	Perp.						
7.23	18	-	42	-	33	-	285	-	52	171	2	8m/7m	11mm	Nothing
7.25	67	64	98	65	82	53	453	255	52	271	1	8m	8mm	Nothing
7.27	125	111	175	109	152	85	682	378	-	1415	0	Grow	Broadening	Nothing
7.29	181	165	258	171	223	127	951	543	-	1615	0	Grow	Broadening	Nothing
7.31	240	225	341	234	294	173	1295	1265	-	1793	-	Grow	Broadening	collapse
8.1	272	255	385	271	336	199	778	1302	-	1875	-	Grow	Broadening	collapse
8.3	339	311	481	346	422	247	557	2232	-	1732	-	Grow	Broadening	Partial collapse
8.5	396	413	587	451	525	313	587	2575	-	5143	-	Grow	Broadening	Partial collapse
8.7	482	439	686	532	613	356	971	2983	-	1972	-	Grow	Broadening	Partial collapse
8.9	551	509	782	624	703	411	995	3322	-	1963	-	Grow	Broadening	Partial collapse

To analyze the impact of reservoir water level changes on coastal landslides, a trend chart was drawn showing the changes in the reservoir water level between May 29 and July 20, as shown in Figure 6. At 8:00 a.m. on May 29, the water level was 1020.25 m, and by 8:00 a.m. on July 20, the reservoir water level had risen to 1118.51 m.

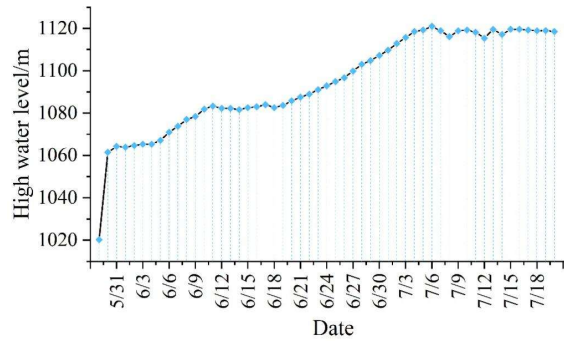


Figure 6: Sequence diagram of water level time of the power station

In summary, the dynamic monitoring model proposed in this paper can detect changes in water volume in real time, thereby achieving the purpose of water level early warning.

IV. C. Deformation analysis of landslide bodies in hydropower reservoir areas

IV. C. 1) Comparative analysis of fiber optic monitoring results for different models

Three different types of optical fibers, designated as f1, f2, and f3, were installed. A comparative analysis of the monitoring results for these three types of optical fibers was first conducted. The test diagrams for optical fibers f1 and f2 are shown in Figure 7. These two optical fibers were completely synchronized from the start of installation. However, due to insufficient cable core length in the loop transmission segment, f2 was laid separately to the monitoring station, resulting in an 8-meter difference in distance between the two. From the test graphs, it can be seen that the two fiber optic cables are of different models, and the absolute strain test values between them differ significantly, indicating that the initial strain of the fiber optic cables during installation was different. However, the sensor segment lengths they reflect are completely consistent. Fiber optic cable 3 was installed synchronously with f1 and f2 starting from the front slope segment a.

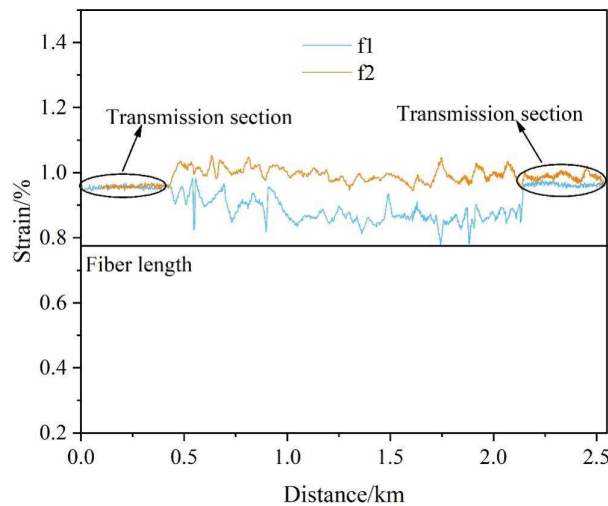


Figure 7: The test graphics comparison of fiber optic f1 and f2

The comparison diagram of the relative strain measured by optical fibers f1, 2, and tube 3 is shown in Figure 8. The figure shows that the relative strain measured by the three optical fibers is relatively small and basically consistent, but there is a large difference between f1 and 2 and f in the exposed section at the top of the anti-slip pile.

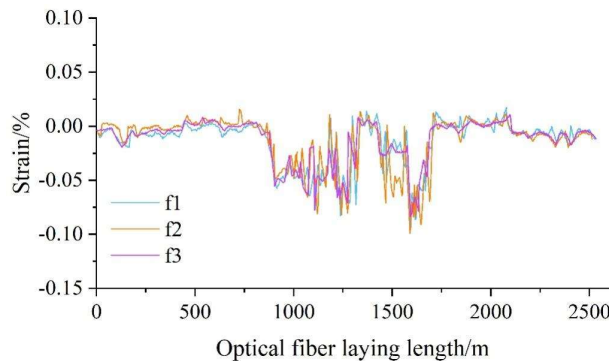


Figure 8: F1, F2 and F3 are corresponding strain comparison diagrams

From the results of the comparative analysis of the test graphs, it can be seen that although the fiber optic cable models are different, the measured relative results are consistent. In practical applications, since the deformation of the slope is reflected through the relative deformation of the fiber optic cable, there is no need to calibrate the fiber optic cable.

Since early January 2020, surface deformation monitoring of the landslide in the reservoir area of the hydropower station has been conducted for a period of three years. During the monitoring process, fiber optic cable f1 broke in early 2021, and fiber optic cable f2 broke in October 2021. The remaining fiber optic cables continued to perform their monitoring functions effectively. Figure 9 shows a comparison of the monitoring graphs from 2020, 2021, and 2022. The comparison results indicate that the deformation of the landslide in the reservoir area of the hydropower station was relatively significant between 2020 and 2021; however, in 2022, the relative deformation detected by monitoring was not prominent, and no significant abnormal deformation of the landslide was observed during the deformation monitoring process.

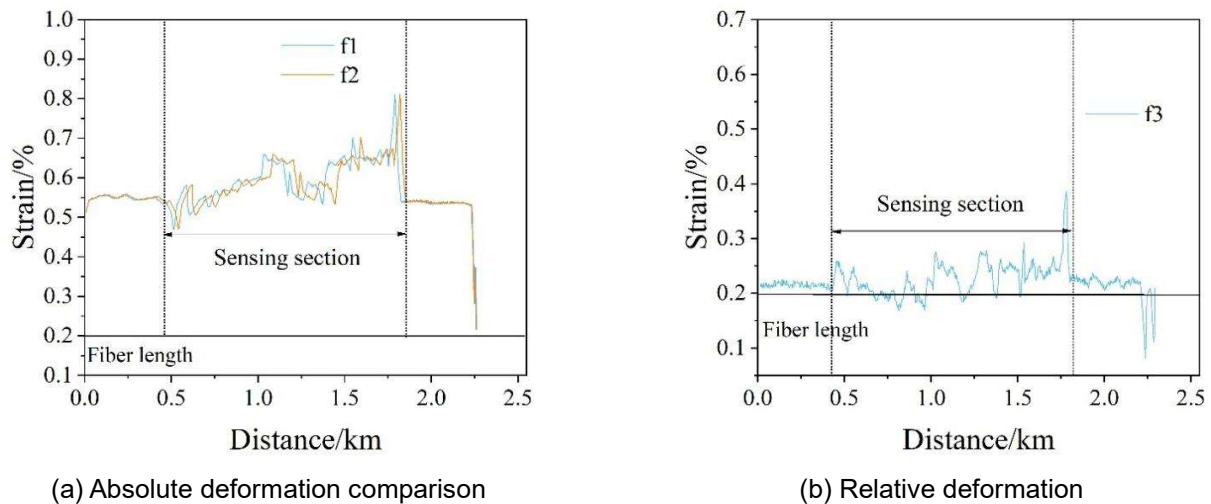


Figure 9: Comparison of monitoring data in January 2020 and November 2022

Monitoring results indicate that after the completion of the remediation project, the overall deformation of the landslide in the reservoir area of the hydropower station was insignificant, and the slope stability was good.

IV. C. 2) Analysis of fiber optic changes in subsidence areas

See Figure 10. The f1, f2, and f3 optical fibers are laid synchronously on the slope using an embedded method. The break points of the optical fibers are located on the slope surface above the slope unloading area, where the medium is loose. When laying the optical fibers, a trench is first dug and then backfilled, resulting in a looser medium at the fiber laying site. During the rainy season, prolonged and repeated rainfall erosion forms gullies on the slope surface, reducing the cohesion of the surrounding soil and causing localized collapses. At the collapse sites, the optical fibers break due to excessive stress.

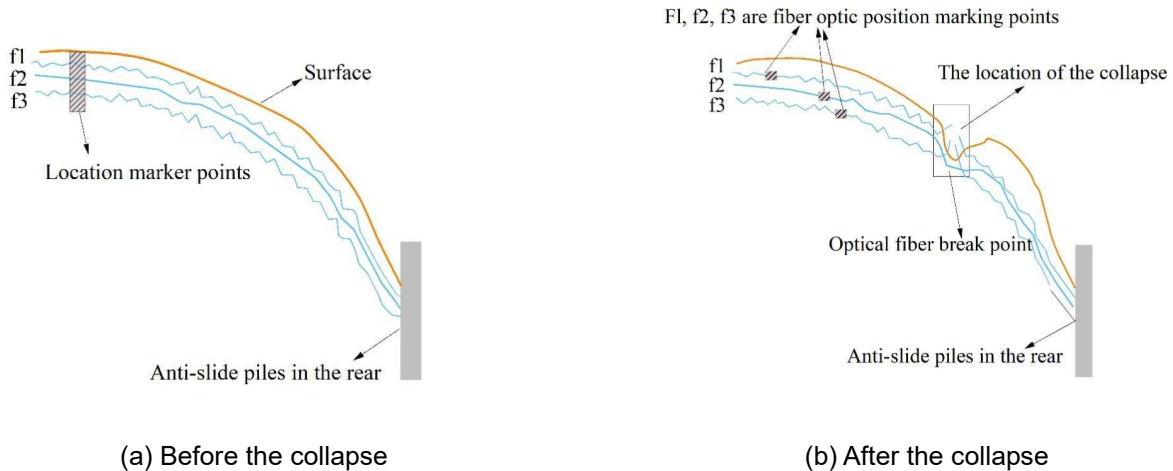


Figure 10: Schematic diagram of optical fiber change before and after collapse

IV. C. 3) Analysis of slope fiber characteristics

Since the slope surface has already undergone mesh spraying treatment during fiber optic cable installation, inserting the fiber optic cable into the medium on the slope surface presents certain challenges. Additionally, excavating trenches on the slope surface is detrimental to slope stability and may damage the vegetation on the slope. Therefore, the installation of fiber optic cables on the slope surface adopts the concept of quasi-distributed fiber optic monitoring, with fiber optic cables fixed at both ends of the slope surface. Since the outer diameter of the f1 fiber is relatively small, it is difficult to secure it with clamps alone. If the f1 fiber is laid simultaneously with the f3 fiber, this effectively increases the outer diameter of the fiber, allowing the clamps to secure both the f1 and f3 fibers. The f2 fiber is laid in a relaxed state along the f1 and f3 fiber routes, serving as a temperature compensation fiber.

The strain changes of the f2 fiber during six consecutive tests are shown in Figure 11. The strain changes of the fiber at different time points are significant. Since the fiber is in a relaxed state, its strain changes are primarily influenced by temperature variations. This indicates that slope temperature changes significantly affect fiber strain. The strain along the fiber exhibits a nearly blind-line distribution, which also suggests that the temperature field on the slope is relatively uniform, with minimal temperature differences along the fiber.

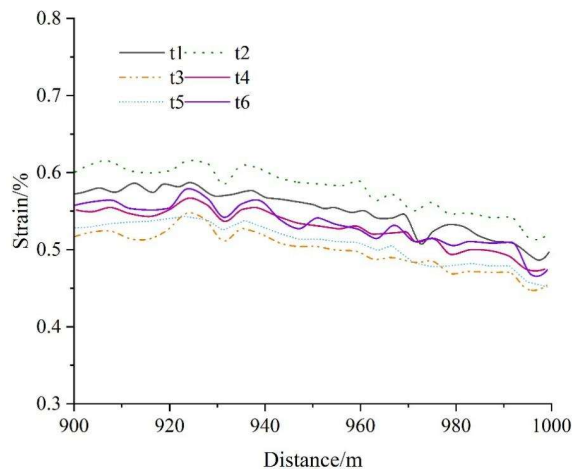


Figure 11: f2 fiber monitoring strain diagram on the slope

Figure 12 shows the strain test results for the f3 fiber optic cable at 850–1050 m. The figure depicts the strain changes over six consecutive slope sections. During fiber optic cable installation, the local section of the cable between two fixed points comes into contact with the slope surface, causing friction and resulting in uneven stress distribution. The strain curve exhibits a wavy pattern. Monitoring results indicate that the overall deformation on the slope surface is minimal, with good stability. The deformation trend aligns with the strain change trend in the

temperature compensation section. Local deformation differences cause the monitoring curve to exhibit a wavy characteristic.

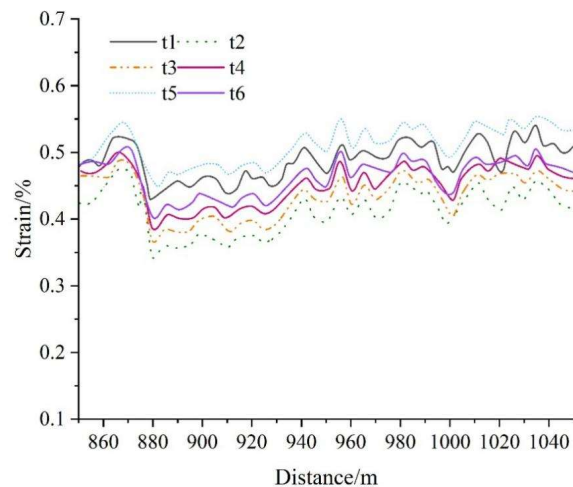


Figure 12: f3 fiber optic strain monitoring on the slope

The results of fiber optic monitoring in two temperature-compensated sections indicate that the strain on the fiber optic cable on the slope surface is significantly affected by temperature. Therefore, temperature compensation should be considered during the installation of the fiber optic cable. The impact of temperature changes within the slope structure on strain changes when the fiber optic cable breaks can be neglected. Additionally, loose-tube fiber optic cables directly embedded into the slope structure can serve a certain sensing function. Therefore, when using loose fibers for direct temperature compensation, if the fibers are implanted into the monitoring object, an additional hard material isolation device must be added around the fibers to ensure they remain in a free state unaffected by medium stress. Additionally, the material of the device should have good thermal conductivity.

V. Conclusion

Based on distributed fiber optic monitoring technology and fiber optic grating sensing technology, this study proposes a fiber optic grating sensing tube deformation calculation method based on the conjugate beam method. On this basis, a deformation monitoring model for landslide bodies in hydropower reservoir areas is established. By monitoring changes in fiber strain and applying field methods, the model's performance characteristics for monitoring deformation of landslide bodies in hydropower reservoir areas are investigated, leading to the following conclusions:

(1) The fiber optic sensing network is highly sensitive to surface deformation, capable of detecting extremely small external forces, and can precisely locate deformation zones and calculate the displacement of each node on the surface through strain analysis.

(2) The monitoring method proposed in this paper can monitor water level changes in real time, providing real-time data for monitoring personnel to develop early warning plans during actual monitoring.

(3) By embedding optical fibers into the slope body and fixing them on the slope surface, the deformation of the slope is directly sensed. It was found that the strain of optical fibers on the slope surface is significantly affected by temperature, while loose-tube optical fibers directly implanted into the slope body play a certain sensing role.

Funding

This work was supported by Science and Technology Project of State Grid Shaanxi Electric Power Co., Ltd. (5226KY240012).

References

- [1] Chang, J., Li, Y., Yuan, M., & Wang, Y. (2017). Efficiency evaluation of hydropower station operation: A case study of Longyangxia station in the Yellow River, China. *Energy*, 135, 23-31.
- [2] Guo, W., & Zhu, D. (2018). A review of the transient process and control for a hydropower station with a super long headrace tunnel. *Energies*, 11(11), 2994.
- [3] Jadoon, T. R., Ali, M. K., Hussain, S., Wasim, A., & Jahanzaib, M. (2020). Sustaining power production in hydropower stations of developing countries. *Sustainable Energy Technologies and Assessments*, 37, 100637.
- [4] Xu, N., Wu, J., Dai, F., Fan, Y., Li, T., & Li, B. (2018). Comprehensive evaluation of the stability of the left-bank slope at the Baihetan hydropower station in southwest China. *Bulletin of Engineering Geology and the Environment*, 77, 1567-1588.

- [5] Shi, G., Gu, G., Zhou, H., Tao, Z., Pan, H., & Tang, T. (2020). Stability monitoring and analysis of high and steep slope of a hydropower station. *Geofluids*, 2020(1), 8840269.
- [6] Wen, F., Song, C., Li, Z., Yu, C., Chen, B., Du, J., ... & Wen, Y. (2025). Landslide detection and deformation control analysis in the reservoir area of Wudongde Hydropower Station by InSAR observations. *Earth and Space Science*, 12(4), e2024EA004002.
- [7] Zhang, Y., Shi, X., Jin, Y., Zhang, S., & Wu, Y. (2025). Displacement characterization of active landslides near the Gushui Hydropower Station using multi-temporal SAR imageries. *Landslides*, 1-15.
- [8] Zhu, H. H., Ye, X., Pei, H. F., Zhang, W., Cheng, G., & Li, Z. L. (2024). Probing multi-physical process and deformation mechanism of a large-scale landslide using integrated dual-source monitoring. *Geoscience Frontiers*, 15(2), 101773.
- [9] Xie, M., Huang, J., Wang, L., Huang, J., & Wang, Z. (2016). Early landslide detection based on D-InSAR technique at the Wudongde hydropower reservoir. *Environmental earth sciences*, 75, 1-13.
- [10] Liang, R., Mei, Y., Yang, X., Xu, J., Zhang, J., & Qin, Q. (2022, March). Distributed temperature monitoring of a pumped-storage power station rockfill dam using optical fiber sensors. In *Eighth Symposium on Novel Photoelectronic Detection Technology and Applications* (Vol. 12169, pp. 828-833). SPIE.
- [11] Hisham, H. K. (2018). Optical fiber sensing technology: basics, classifications and applications. *Am. J. Remote Sens*, 6(1), 1-5.
- [12] Pendão, C., & Silva, I. (2022). Optical fiber sensors and sensing networks: overview of the main principles and applications. *Sensors*, 22(19), 7554.
- [13] Lu, P., Lalam, N., Badar, M., Liu, B., Chorpeneing, B. T., Buric, M. P., & Ohodnicki, P. R. (2019). Distributed optical fiber sensing: Review and perspective. *Applied physics reviews*, 6(4).
- [14] Schenato, L. (2017). A review of distributed fibre optic sensors for geo-hydrological applications. *Applied Sciences*, 7(9), 896.
- [15] Joe, H. E., Yun, H., Jo, S. H., Jun, M. B., & Min, B. K. (2018). A review on optical fiber sensors for environmental monitoring. *International journal of precision engineering and manufacturing-green technology*, 5, 173-191.
- [16] Ye, X. W., Su, Y. H., & Han, J. P. (2014). Structural health monitoring of civil infrastructure using optical fiber sensing technology: A comprehensive review. *The Scientific World Journal*, 2014(1), 652329.
- [17] Elsherif, M., Salih, A. E., Muñoz, M. G., Alam, F., AlQattan, B., Antonysamy, D. S., ... & Butt, H. (2022). Optical fiber sensors: Working principle, applications, and limitations. *Advanced Photonics Research*, 3(11), 2100371.
- [18] Ren, L., Jiang, T., Jia, Z. G., Li, D. S., Yuan, C. L., & Li, H. N. (2018). Pipeline corrosion and leakage monitoring based on the distributed optical fiber sensing technology. *Measurement*, 122, 57-65.
- [19] Zheng, Y., Zhu, Z. W., Li, W. J., Gu, D. M., & Xiao, W. (2019). Experimental research on a novel optical fiber sensor based on OTDR for landslide monitoring. *Measurement*, 148, 106926.
- [20] Ivanov, V., Longoni, L., Ferrario, M., Brunero, M., Arosio, D., & Papini, M. (2021). Applicability of an interferometric optical fibre sensor for shallow landslide monitoring—Experimental tests. *Engineering Geology*, 288, 106128.
- [21] Johnson, M. A. M., Phang, S. K., Wong, W., Chew, W. J. E. N., Mun, H. K. I. T., & Hoon, Y. (2023). Distributed fiber optic sensing landslide monitoring—a comparative review. *J Eng Sci Technol*, 18(1), 406-423.
- [22] Cheng, L., Pan, P., Sun, Y., Zhang, Y., & Cao, Y. (2023). A distributed fibre optic monitoring method for ground subsidence induced by water pipeline leakage. *Optical Fiber Technology*, 81, 103495.
- [23] Rabaiotti, C., Höttges, A., Facchini, M., & Bohren, I. (2023, June). FIBRADIKE, a novel distributed fiber optic monitoring system for dikes and earth dams. In *IOP Conference Series: Earth and Environmental Science* (Vol. 1195, No. 1, p. 012004). IOP Publishing.
- [24] Li, H., & Yang, M. (2024). Application study of distributed optical fiber seepage monitoring technology on embankment engineering. *Applied Sciences*, 14(13), 5362.
- [25] Ye, X., Zhu, H. H., Wang, J., Zhang, Q., Shi, B., Schenato, L., & Pasuto, A. (2022). Subsurface multi - physical monitoring of a reservoir landslide with the fiber - optic nerve system. *Geophysical Research Letters*, 49(11), e2022GL098211.
- [26] Jia, H., Zhang, H., Liu, L., & Liu, G. (2019). Landslide deformation monitoring by adaptive distributed scatterer interferometric synthetic aperture radar. *Remote Sensing*, 11(19), 2273.
- [27] Wijaya, H., Rajeev, P., & Gad, E. (2021). Distributed optical fibre sensor for infrastructure monitoring: Field applications. *Optical Fiber Technology*, 64, 102577.
- [28] Acharya, A., & Kogure, T. (2023). Application of novel distributed fibre-optic sensing for slope deformation monitoring: a comprehensive review. *International Journal of Environmental Science and Technology*, 20(7), 8217-8240.
- [29] Minardo, A., Zeni, L., Coscetta, A., Catalano, E., Zeni, G., Damiano, E., ... & Olivares, L. (2021). Distributed optical fiber sensor applications in geotechnical monitoring. *Sensors*, 21(22), 7514.
- [30] Inaudi, D. (2019). Optical fiber sensors for dam and levee monitoring and damage detection. *Levees and dams: advances in geophysical monitoring and characterization*, 91-120.
- [31] Schenato, L., Palmieri, L., Camporese, M., Bersan, S., Cola, S., Pasuto, A., ... & Simonini, P. (2017). Distributed optical fibre sensing for early detection of shallow landslides triggering. *Scientific Reports*, 7(1), 14686.
- [32] Inaudi, D., & Blin, E. R. (2016, September). Monitoring dams with distributed fiber optic sensing. In *Proceedings of the International Conference on Dam Engineering*, Philadelphia, PA, USA (pp. 11-14).
- [33] Zhou, S., Chen, B., Lu, H., Shan, Y., Li, Z., Li, P., ... & Li, W. (2023). Analysis of the spatial distribution and deformation types of active landslides in the upper Jinsha River, China, using integrated remote sensing technologies. *Remote Sensing*, 16(1), 100.
- [34] Zhu, H. H., Shi, B., Zhang, L., & Ye, X. (2021, March). Fiber Optic Monitoring and Forecasting of Reservoir Landslides. In *International Workshop on Civil Structural Health Monitoring* (pp. 1-13). Cham: Springer International Publishing.
- [35] Wang, J., Zhang, S., Lv, T., Liu, Y., & Ji, K. (2024, May). MethodApplication of Distributed Optical Fiber Brillouin Sensing in Slope Monitoring. In *2024 IEEE 6th Advanced Information Management, Communicates, Electronic and Automation Control Conference (IMCEC)* (Vol. 6, pp. 251-254). IEEE.
- [36] Liu, T., Li, Q., Li, X., Tan, Y., & Cao, X. (2024). A critical review of distributed fiber optic sensing applied to geologic carbon dioxide storage. *Greenhouse Gases: Science and Technology*, 14(4), 676-694.
- [37] Soga, K., & Luo, L. (2018). Distributed fiber optics sensors for civil engineering infrastructure sensing. *Journal of Structural Integrity and Maintenance*, 3(1), 1-21.



- [38] Mahsa Gharizadehvarnosefaderani, Md. Fazle Rabbi, Cameron D. Stuart & Debakanta Mishra. (2025). Performance evaluation of rail-mounted quasi-distributed optical fiber sensors for monitoring track transitions. *Transportation Geotechnics*, 51, 101487-101487.
- [39] Dandan Sun, Jingru Mao, Miao Liu, Hanlin Liu, Shoupeng Zhang, Binglin Li... & Jie Ma. (2025). A fiber Bragg grating (FBG)-strain sensing tube for deep displacement measurement. *Optics and Laser Technology*, 188, 112938-112938.